



Motions of CMS detector structures due to the magnetic field forces as observed by the Link alignment system during the test of the 4 T magnet solenoid

L.A. García-Moral^a, G. Gómez^a, F.J. González-Sánchez^a, C. Martínez-Rivero^a, F. Matorras^a, T. Rodrigo^a, P. Martínez^a, L. Scodellaro^a, I. Vila^a, A.L. Virto^a, M. Sobrón^{a,*}, J. Alberdi^b, P. Arce^b, J.M. Barcala^b, E. Calvo^b, A. Ferrando^b, M.I. Josa^b, A. Molinero^b, J. Navarrete^b, J.C. Oller^b, C. Yuste^b, N. Béni^c, P. Raics^c, Zs. Szabó^c, Z. Trócsnyi^c, B. Ujvári^c, Gy. Zilizi^c, G. Christian^d, J. Imrek^d, J. Molnár^d, D. Novák^d, J. Pálkás^d, G. Székely^d, Z. Szillási^d, G.L. Bencze^e, G. Vesztergombi^e, A. Calderón^f, M. Benettoni^f, F. Gasparini^f, F. Montecassiano^f, M. Rampazzo^f, M. Zago^f, A. Benvenuti^g

^a Instituto de Física de Cantabria (IFCA), CSIC-Universidad de Cantabria, Santander, Spain

^b Centro de Investigaciones Energéticas Medioambientales y Tecnológicas (CIEMAT), Madrid, Spain

^c University of Debrecen, Institute of Experimental Physics, Debrecen, Hungary

^d Institute of Nuclear Research ATOMKI, Debrecen, Hungary

^e KFKI Research Institute for Particle and Nuclear Physics, Budapest, Hungary

^f Dipartimento di Fisica dell'Università di Padova e Sezione dell'INFN, Padova, Italy

^g Dipartimento di Fisica dell'Università di Bologna e Sezione dell'INFN, Bologna, Italy

ARTICLE INFO

Article history:

Received 11 March 2009

Accepted 26 March 2009

Available online 16 April 2009

Keywords:

Alignment

CMS

Detectors

ABSTRACT

This document describes results obtained from the Link alignment system data recorded during the Compact Muon Solenoid (CMS) Magnet Test. A brief description of the system is followed by a discussion of the detected relative displacements (from micrometres to centimetres) between detector elements and rotations of detector structures (from microradians to milliradians). Observed displacements are studied as functions of the magnetic field intensity. In addition, the reconstructed positions of active element sensors are compared to their positions as measured by photogrammetry and the reconstructed motions due to the magnetic field strength are described.

© 2009 Elsevier B.V. All rights reserved.

1. Introduction

From the point of view of muon measurement, the Compact Muon Solenoid (CMS) Detector [1–3] is a muon spectrometer and the detection of these particles is favoured. Attending to the magnet field intensity, two different technologies are employed for their measurement. In the barrel region, surrounding the coil of the solenoid, four layers of drift chambers, interleaved with the return iron yoke, make a redundant measurement of the muon momenta. A muon chamber is made of three superlayers. Each superlayer is made of four layers of drift cells. The drift cell is the basic unit measuring the drift time of a muon, providing a spatial resolution of 250 μm . Each superlayer will contribute with the measurement of one coordinate. Two superlayers measure the $r\phi$ coordinate and one layer measures the z coordinate. The

mechanical design of a drift chamber is driven by the precision in the determination of a point of the muon track, 100 μm , which is obtained by a fit of the individual hits in each cell.

The muon drift chambers will be subject to variable residual magnetic fields, below 0.4 T for all the chambers except for the MB1 chambers near the endcaps. There, the magnetic field will rise up to 0.8 T. In the region of the ME1/1 chambers the field will be $B_z \approx 3$ T. For such magnetic field intensity the operation of the muon drift chambers is limited, since the drift cell escapes the linear regime. CMS uses, at the endcaps, other gaseous detectors called Cathode Strip Chambers (CSCs) that can operate in large and non-uniform magnetic fields without significant deterioration of performance. CSCs are multiwire proportional chambers in which one cathode plane is segmented into strips running across wires, both of them instrumented, giving 2D information of the particle passage. Due to the intense magnetic field, the muon trajectories bend more in the vicinity of the first endcap station where the higher precision is required (75 μm). For the rest of the chambers the precisions will be of about 150 μm .

* Corresponding author.

E-mail address: sobron@ifca.unican.es (M. Sobrón).

The measurement of the muon momentum is related to its bending in the transverse plane. The radius of curvature (ρ) and the momentum perpendicular to the magnetic field (p_t) of a muon are related by $\rho(\text{m}) = p_t(\text{GeV}/c)/0.3B(\text{T})$. The radius of curvature can be obtained from the measurement of the muon trajectory sagitta s , after traversing a distance d in the magnetic field, using the approximate expression $\rho = d^2/8s$.

An error in the measurement results in an error in the momentum measurement. The relative error in the sagitta measurement is $\delta s/s = \delta p_t/p_t \approx \sigma_s(\text{mm})p_t(\text{TeV})/d^2(\text{m}^2)B(\text{T})$, where σ_s is the resolution in the sagitta measurement. The relative resolution deteriorates with the muon momentum and improves linearly with the magnetic field and quadratically with the traversed distance.

The accuracy required in the position of the muon chambers is determined by the resolution demanded in the reconstruction of the momentum of high energy muons. CMS is designed to achieve a combined (tracker and muon systems) momentum resolution for the region $|\eta| < 2.4$ of 0.5–1% for $p_t \approx 10\text{ GeV}$, 1.5–5% for $p_t \approx 100\text{ GeV}$ and 5–20% for $p_t \approx 1\text{ TeV}$. This design accuracy will require the knowledge of the position of the chambers with a precision comparable to their resolution.

In order to quantify the importance of the chambers misalignment in the momentum resolution, several simulation studies have been performed [4]. As a result, for the most important coordinate from the physics point of view, $(r\phi)$ the alignment system should reconstruct the position of the chambers within a 150–300 μm range for MB1–MB4 and within a 75–200 μm range for ME1–ME4. The constraints are tighter for ME1 and MB1 since most muons reach the maximum curvature near the first muon station. These stations give the main contribution to the momentum measurement precision and therefore their chambers SET the requirements of measurement resolution and position accuracy.

However, the stability of the muon chambers at the level of 100 μm is not guaranteed at all when CMS enters in operation. The expected movements and deflections of the muon spectrometer will exceed this value. To monitor these movements, CMS is instrumented with an opto-mechanical alignment system that

allows the continuous measurement of the position of the chambers. The system provides precise information on the relative position of the muon chambers amongst themselves (in the barrel and endcaps), as well as on the position of the muon chambers with respect to the tracker, assumed to be a rigid body. The information provided by the alignment will be used for off-line corrections in the track reconstruction.

A test of part of the alignment system [3] was carried out in summer and autumn of 2006 when the CMS four-Tesla Magnet was commissioned. The test (Magnet Test and Cosmic Challenge, MTCC) took place in two different phases in the SX5 assembly hall at CERN. Several components of the muon detector were also tested with cosmic rays [5].

This document is organized as follows: the CMS muon alignment system is briefly described in Section 2. In Section 3 we summarize the parts of the system installed and tested during the MTCC period. Details on data acquisition, detector control system (DCS) and data flow are given in Section 4. A general overview of the results obtained from the data recorded by the Link alignment system is shown in Section 5. Section 6 is devoted to a detailed analysis of the data quality and observed displacements of the different sensors used in the system. Section 7 introduces the software package used for geometrical reconstruction: COCOA (CMS Object Oriented Code for Optical Alignment [6]), and the results obtained from a full reconstruction are presented. Summary and conclusions are given in Section 8.

2. The CMS alignment system

An overall layout of CMS is shown in Fig. 1. At the heart of CMS, a 13 m long, 6 m inner diameter, 4 T superconducting solenoid provides a large bending power: 12 Tm. The return field is large enough to saturate 1.5 m of iron, allowing four muon stations to be integrated to ensure robustness and full geometrical coverage.

The muon system consists of about 25 000 detection planes embedded in the 15 m diameter, 20 m long return yoke. To cope with all the muon momentum resolution requirements explained in the Introduction, the system is instrumented with a complex

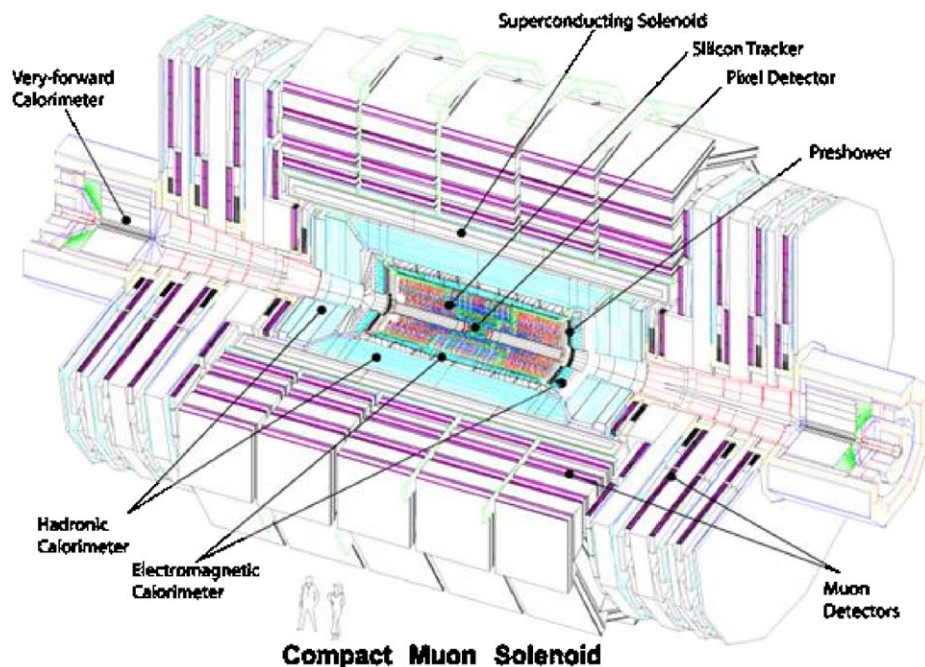


Fig. 1. A perspective view of the CMS detector.

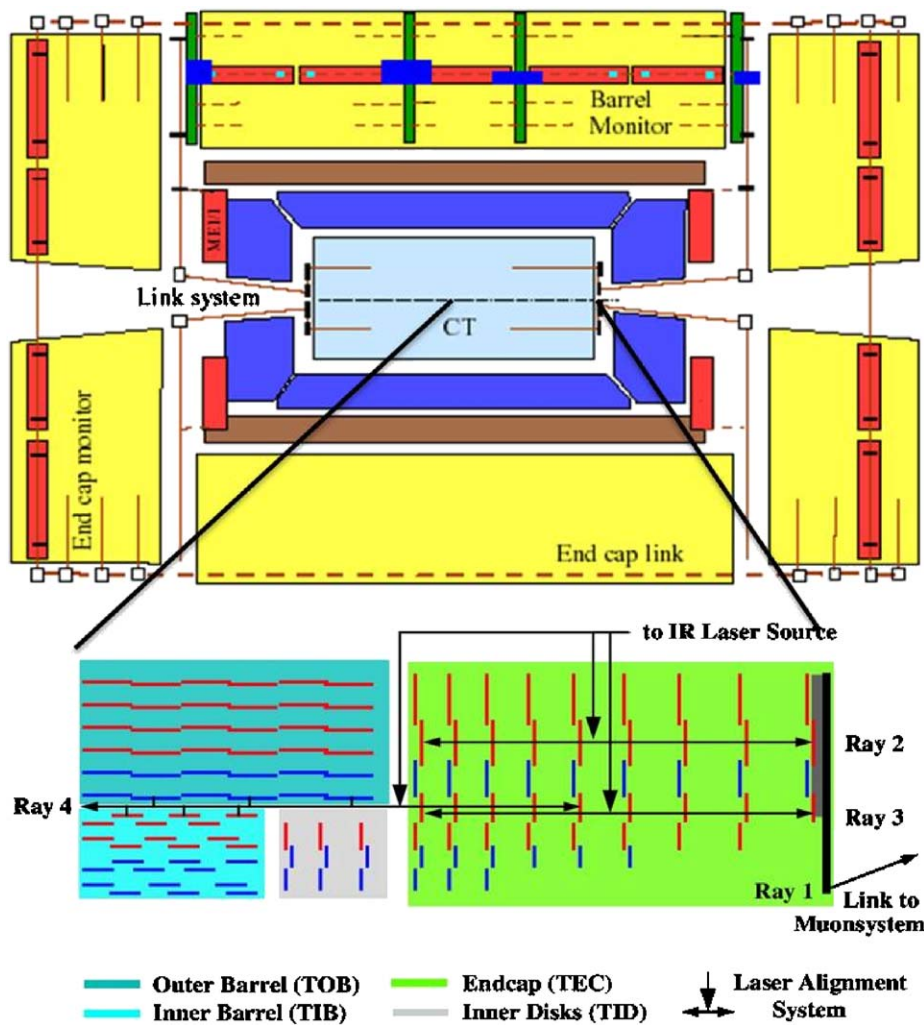


Fig. 2. One of the ϕ planes showing the three alignment subsystems.

opto-mechanical alignment system organized in three basic blocks:

- The tracker internal alignment, to measure the positions of the various modules and monitor the eventual internal deformations.
- The muon systems (barrel and endcaps) internal alignment, to monitor the relative position among the chambers.
- The Link system, to relate the position of the various elements of the muon system (barrel and endcaps) with the position of the tracker body, and to monitor the relative movements between both systems.

We show in Fig. 2 one of the ϕ alignment planes where the three alignment subsystems can be seen. There are in total three ϕ planes. Each plane contains four independent alignment quarters where the three systems are connected.

2.1. The tracker alignment

The alignment of the tracker units (silicon sensors) is done with internal laser beams. The Laser Alignment System (LAS) [7] uses infrared laser beams to monitor the position of selected tracker modules. It operates globally on tracker substructures and cannot determine the position of individual modules. The goal of the system is to generate alignment information on a continuous

basis, providing the geometry of the tracker substructures at the level of $100\ \mu\text{m}$. In addition, possible tracker structure movements can be monitored at the level of $10\ \mu\text{m}$ using offline alignment algorithms based on the information of the tracks crossing the detectors.

In each tracker endcap structure (TEC), eight axial laser beams, distributed in r and ϕ , cross all nine endcap discs. At each TEC end-face, three mechanical supports—pillars—rigidly attached to the most external (ninth) disc transfer the internal tracker geometry information to the outside world. The relation between the position of the tracker body and the muon chambers (barrel and endcaps) is obtained through the Link system, in particular by means of 12 laser beams housed on two carbon-fibre structures (Alignment Rings, AR) which are supported by the three TEC pillars at each end of the tracker. The position and orientation of each AR is therefore known precisely in the tracker coordinate system. The goal is to monitor motions of the muon structures with respect to the tracker system with an accuracy of about $200\ \mu\text{m}$.

2.2. The barrel alignment

The barrel alignment system [3] measures the positions of the barrel muon chambers with respect to each other and to the entire barrel muon spectrometer (see sketch in Fig. 3). Each barrel muon chamber is equipped with light sources (LEDs, more than

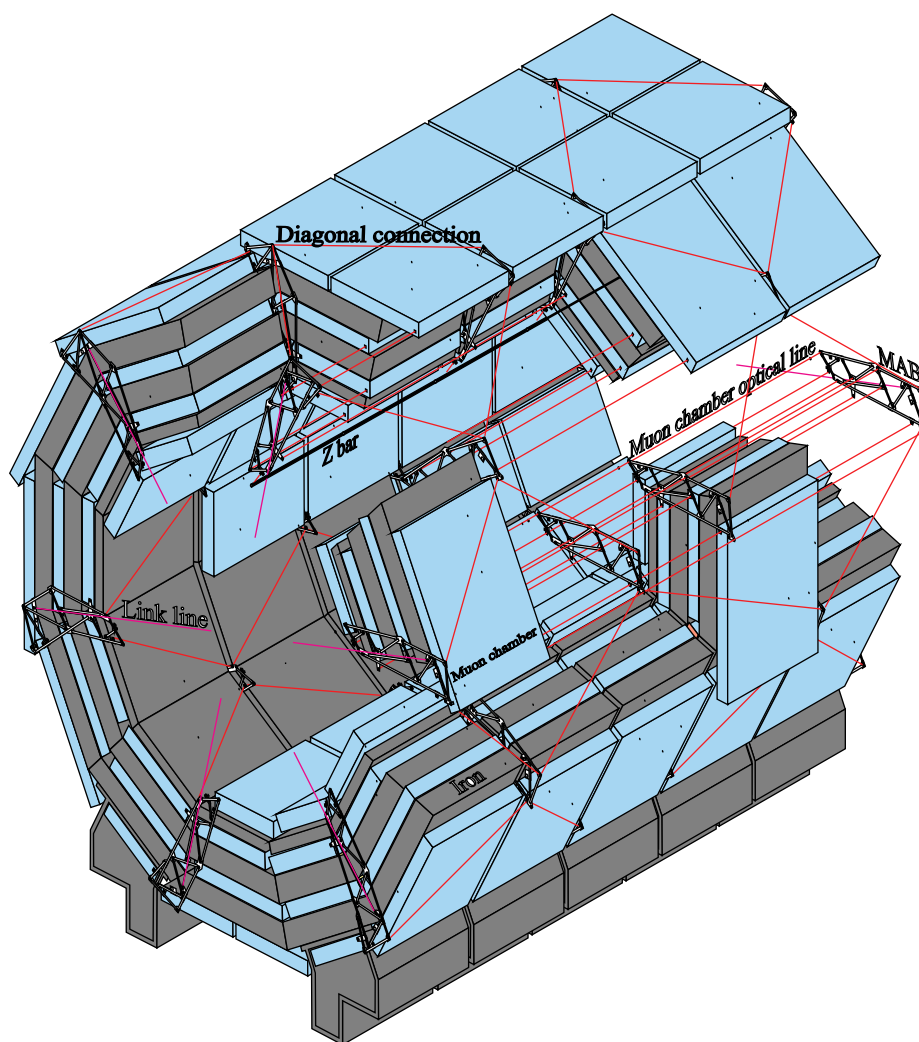


Fig. 3. The barrel muon alignment system.

9000 in total). The LEDs are observed by small video-cameras (600 in total) mounted on rigid carbon-fibre structures called MABs (Module for the Alignment of the Barrel). There are direct observations between the MABs called diagonal connections. The system is completed with long carbon-fibre bars called z-bars fixed to the vacuum-tank of the magnet. The z-bars (12 in total, six per side) are also equipped with LED light sources and observed by video-cameras mounted on the MABs. The MABs (36 altogether) are fixed to the return yoke in the gaps between the barrel wheels (six per gap) and on both ends of the barrel (six per side). The MABs on the two ends, containing Link and endcap elements, are used to connect the three alignment subsystems to each other.

2.3. The endcap alignment

The endcap alignment system [1,3,8,9] is designed to monitor the relative positions of the CSC chambers. The system uses a complex arrangement of five types of sensors for the transferring and monitoring of the ϕ , r , and z coordinates. It measures only a set of selected chambers per layer, in total a sixth of all endcap chambers.

The main monitoring tools within the $r\phi$ plane are the Straight Line Monitors (SLM). Each SLM consists of two cross-hair lasers, which emit a nearly radial laser beam across four chambers from

each end, and provide straight reference lines that are picked up by two optical sensors (Digital CCD Optical Position Sensors, DCOPS) placed at each CSC chamber. The ϕ coordinate alignment is handled by optical SLMs and transfer lines. Transfer lines run parallel to the CMS z -axis along the outer cylinder envelope of CMS at six angles separated 60° in ϕ . Transfer lines provide an optical connection between the full barrel and endcap muon structures.

A visualization of the geometry and components of the muon endcap alignment is shown in Fig. 4 [1,8].

2.4. The Link alignment system

The purpose of the Link alignment system is to measure the relative positions of the muon spectrometer and the tracker body in a common CMS coordinate system. It is designed to work in a challenging environment of very high radiation and magnetic fields, meet tight space constraints, and provide high precision measurements over long distances.

A distributed network of Amorphous Silicon Position Detectors (ASPDs) placed around the muon spectrometer is connected by laser lines. An ASPD sensor [10,11] consists of two groups of 64 silicon micro-strips, with a pitch of $430\mu\text{m}$, oriented perpendicularly. The intrinsic sensor position resolution is better than $5\mu\text{m}$. The centring of the sensor in its mechanical mount was

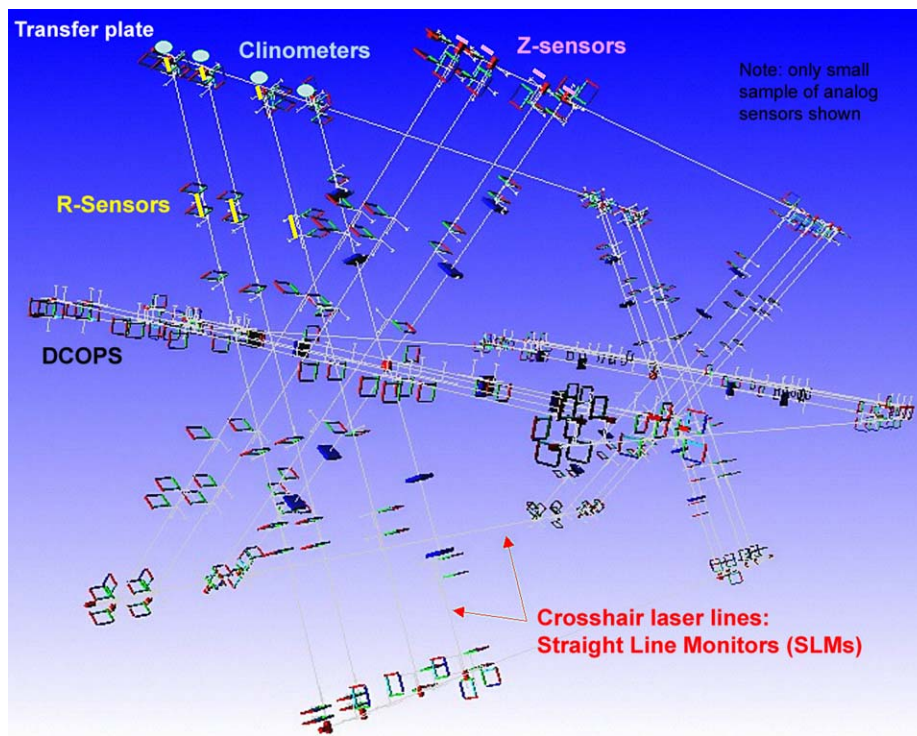


Fig. 4. Visualization of the geometry and components of the muon endcap alignment system. The square objects represent optical sensors (DCOPS) for monitoring three straight laser lines across each endcap station. Axial transfer lines across endcaps are also shown.

measured with 3D and 2D coordinate measuring machines with a precision in the range 5–10 μm .

The entire Link system is divided into three planes 60° apart starting at $\phi = 15^\circ$. Each plane consists of four independent quadrants, resulting in 12 laser paths, or lines: six on each side (positive or negative z) of the CMS detector. Fig. 5 shows a sketch of a quarter of ϕ plane with its instrumentation. The three laser light paths originated at three different regions (tracker, endcap and barrel), are also indicated in Fig. 5. All laser sources—collimators—are housed in carbon-fibre structures called Alignment Rings, MABs, and LDs (Link Disks).

The ARs, rigid carbon-fibre annular structures, are placed at both ends of the tracker as described in Section 2.1. The LDs are suspended from the outer diameter of the YN/1 iron disks of the endcap muon spectrometer by means of aluminium tubes attached to the mechanical assemblies called Transfer Plates (TP). MABs are mounted onto the barrel yoke as described in Section 2.2. Fig. 6 shows the AR and LD installed in CMS.

The ME1/1 and ME1/2 disks of chambers of the endcap muon spectrometer are linked to the tracker and the barrel muons via the laser paths and opto-mechanical sensors installed in the TPs and MABs.

The multiple laser-ASPD link measurement network is complemented by proximity sensors (optical and mechanical). Electrolytic tilt-meters (for angular measurements with respect to the gravity vector of the elements to which they are attached), magnetic and temperature probes, not shown in Fig. 5, are also used by the system.

The monitoring of the relative displacements between some CMS elements relevant for the system (along the light path, z and $r\phi$ directions) is done with the help of aluminium bars (longitudinal and radial profiles, LP and RP, also shown in Fig. 5) for long distances, and contact and non-contact proximity sensors

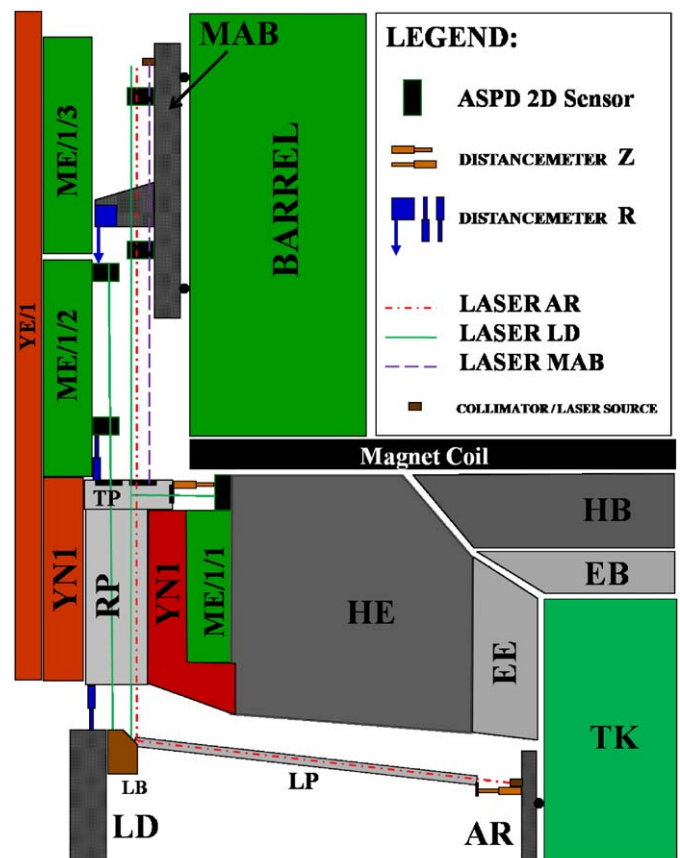


Fig. 5. Link alignment elements in a quarter of ϕ plane.

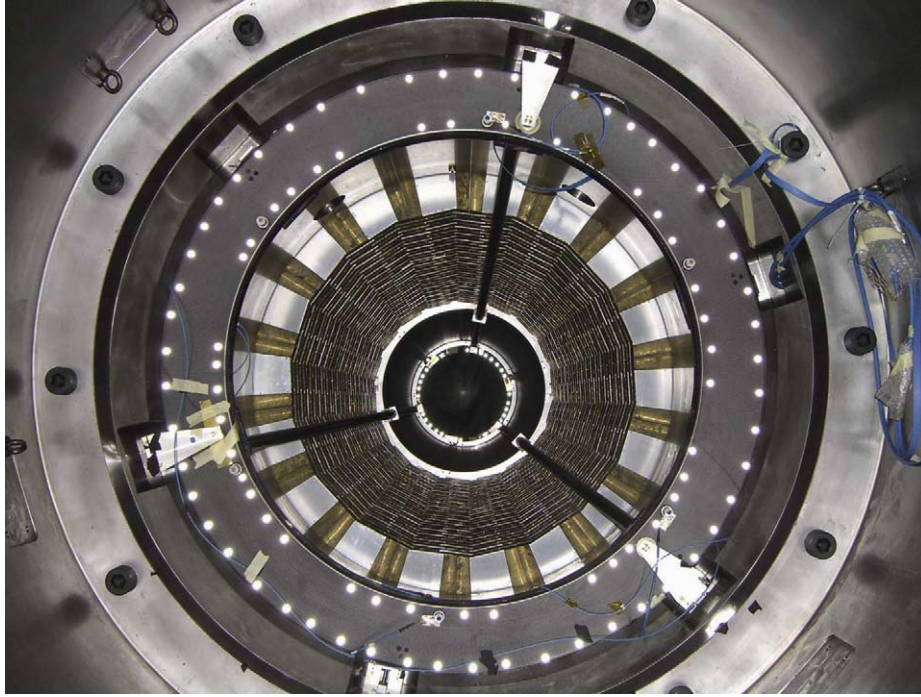


Fig. 6. Photograph of the Link disk—larger disk at the front—and the Alignment Ring—smaller ring in the back—from the +z CMS axis.

for short distances. Changes in length of the aluminium profiles due to temperature variations are controlled by the appropriate temperature probes.

A 3600 mm long profile, LP, relates LD and AR approximately in the region $\eta = 3$. On its end closest to the AR a target is in contact with a potentiometer [12], located at the AR, allowing the monitoring of the relative distance between LD and AR structures along the CMS z coordinate at three different ϕ positions. The other z monitoring in a ϕ quarter is the relative distance between the TP and the ME1/1 chamber, which is also measured by a contact potentiometer installed in the TP whose rod touches a target situated on the top side of the ME1/1 chamber (see Fig. 5).

The rest of the relative distance measurements between CMS elements in a ϕ quarter monitor eventual motions in the $r\phi$ direction. The longest monitored distance, between LD and TP, is measured by a 1977 mm long radial profile (RP in Fig. 5) instrumented with a potentiometer in the end closest to the LD. Relative displacements between the TP and the bottom side of the ME1/2 chamber are monitored as well using contact potentiometers. The $r\phi$ relative distance between the MAB structure and the top side of the ME1/2 chamber in the corresponding ϕ quarter is monitored with a non-contact proximity device [13]. A sensor is installed at the bottom part of each MAB structure. The sensor emitting/receiving head directs a laser light and receives the reflected light to/from a target located on the top region of the ME1/2 chamber. All proximity measurements along $r\phi$ are labelled as Distancemeter R in Fig. 5.

Concerning measurement errors, the lengths of the longitudinal profiles are determined with an error smaller than $30\ \mu\text{m}$. The dimensions of the various sensor mechanical supports are measured with a 3D measuring machine with a precision in the range $5\text{--}10\ \mu\text{m}$. The typical precision in the short-distance measurements of the contact and optical sensors used in the Link system stays, according to our bench calibrations [14], in the region $30\text{--}40\ \mu\text{m}$. However, the uncertainty in the spatial location of sensors related to their mounting in CMS is never smaller than $300\ \mu\text{m}$, as measured by survey and photogrammetry techniques.

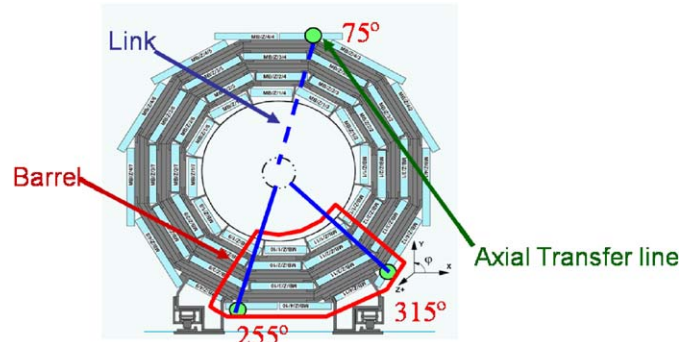


Fig. 7. Transverse view of the muon barrel system with indication of the installed elements in the Magnet Test.

The estimated combined error (mechanical support length plus proximity sensor output plus the mounting uncertainty) in the measurements of absolute positions is about $305\ \mu\text{m}$. Nevertheless, the relative distance measurements are only affected by the precision of the proximity sensors, $40\ \mu\text{m}$.

Complementing the laser and distance measurement system, all the alignment structures (ARs, LDs, TPs, and MABs) are instrumented with different models of tiltmeter sensors [15] which provide direct angular information. Details on their calibrations and measurement precision can be found in Ref. [16].

3. The CMS alignment system elements installed for the Magnet Test

Fig. 7 sketches the geometry of the CMS alignment system operational during the test of the CMS Magnet (MTCC). The system consisted of three Link system quarters of ϕ planes (75° , 255° and 315°) in the positive side of the detector; the full positive endcap alignment system (not shown in the figure), and the full instrumentation of two bottom barrel sectors (Sectors 10 and 11) of the barrel alignment system.

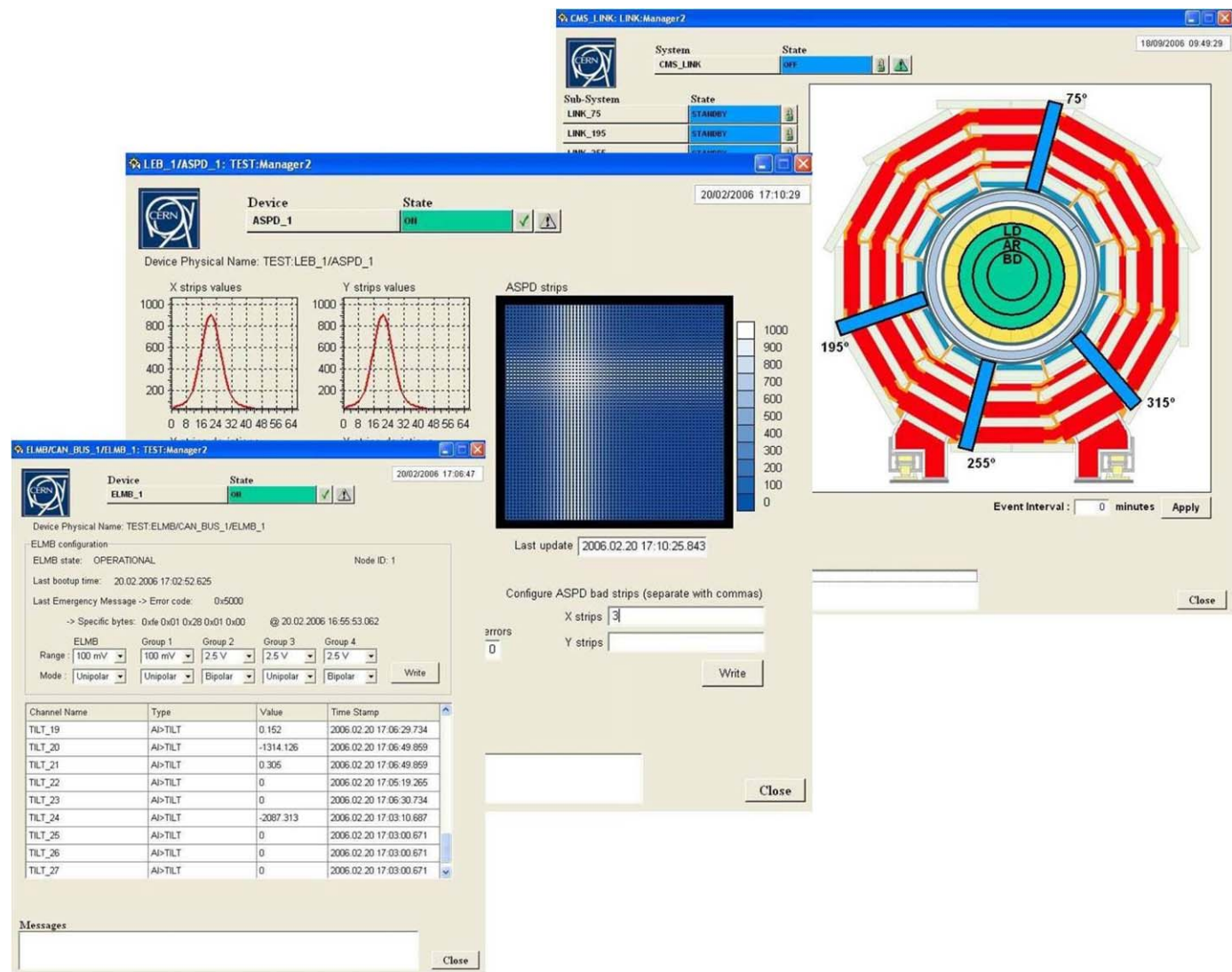


Fig. 8. PVSS monitoring panels (see text).

That arrangement implied the installation of a total of 275 1D sensors (distancemeters and clinometers), 125 photodetectors (DCOPS and ASPDs), 100 video cameras, 534 light sources (LEDs and semiconductor lasers) and a good number of temperature, humidity and magnetic field probes.

During the first part (Phase I) of the Magnet Test a mock-up of the tracker was installed, allowing the installation of the AR, to perform full alignment measurements. Both elements, the tracker mock-up and the AR, were removed for the second part of the test (Phase II) in order to carry out a precise field mapping inside the solenoid.

All components, carbon-fibre structures and all types of sensors were calibrated, previous to their installation, on specific benches, with precisions in the tenths of m for lengths and tenths of rad for angular orientations. In addition, survey and photogrammetry of components were performed during installation with precisions in the 50–300 μm range for spatial positions.

4. Data acquisition and detector control systems

The DAQ and detector control systems are integrated into the detector control system environment. The standard slow control

software adopted by CMS is PVSS, used within a framework called JCOP (Joint Controls Project) which provides a set of guidelines, conventions and common software tools. Hardware devices and sensors are controlled and readout through specialized electronics which communicate with PVSS via the OPC (OLE—Object Linking and Embedding—for Process Control) or DIM (Discrete Information Management) protocols.

All sensors except the ASPDs are controlled through standard ELMB (Embedded Local Monitor Board) cards, for which tools exist within the JCOP Framework for the creation of PVSS data structures which allow easy access and control. ASPDs are read and controlled by custom dedicated electronic cards which are not contemplated in the JCOP Framework. Data structures and PVSS panels are therefore developed specifically for these cards. Fig. 8 shows, as an illustration, three different PVSS panels: one is the general control panel for the Link system and the other two show the monitoring of an ASPD and different 1D distance sensors in a line.

An FSM (Finite State Machine) tool provided in the JCOP Framework facilitates the construction of a hierarchical tree of devices (Device Units) and logical partitions (Control Units) which allow to control and configure the hardware and to coordinate the traffic of commands, states and alarms between different nodes. It

automatically controls the different partitions, states and alarms of each subsystem and allows enabling or disabling any part of the system.

Data taking is not limited to passive recording. Different sequences and reading cycles can be performed for each device by complementing the FSM tree with a PVSS script which coordinates the reading sequences and checks the state of each device. This can also be done through an external script, using Java, to communicate with PVSS via DIM.

As an example, for each ϕ quadrant of the Link system (see Fig. 5), the readout sequence is the following: all lasers from the AR turn on simultaneously for a short time interval (impacting on the TP and MAB sensors). After this, the AR lasers are turned off and all MAB lasers turn on (impacting on the MAB and TP sensors). Finally the MAB lasers are turned off while the LD lasers are turned on (impacting on TP, ME11, ME12 and MAB sensors). This reading cycle (called event) is repeated starting again with the AR lasers. The readout of the proximity and tiltmeter sensors is done in a continuous mode.

Data are recorded in an on-line Oracle database through the use of the RDB (Relational Database) Manager provided by PVSS. The data are subsequently organized and written into Root n-tuples by specialized online scripts which perform database queries, apply calibrations and construct full events for each subsystem. These Root files are then transferred from the private online domain to the Tier-0 and the CAF (offline) by means of the CMS Storage Manager, essentially following the same path as CMS event data, to be used as input by COCOA for offline geometry reconstruction.

5. Overview of results from the Link alignment system during the CMS Magnet Test

The entire Link DAQ and data flow chain was operational during the MT. The data from the different sensors in the system allow a measurement of the relative displacements and deforma-

tions of the yoke structures for the different magnetic field values.

Two main general effects derive from the observation of the MT Link data. The first is the change in the original positions of the structures (the positions before any magnet operation). Compression of the structures along z , towards the interaction point, and deformations in $r\phi$ seem to stabilize after the magnetic field intensity reaches the vicinity of ~ 3.5 T for the first time. These initial displacements and deformations are permanent: they are not recovered in subsequent magnet-off states, and can be interpreted as the final closing of the structures due to the magnetic forces acting on the iron. The magnitude of the measured displacements are understood as specific to the first CMS closing experience and cannot be extrapolated to other scenarios. The second effect is the quasi-elastic deformations between magnet-on and magnet-off states after the permanent compression/deformation is reached. Both effects, permanent and quasi-elastic, can be observed in Figs. 9 and 10.

Fig. 9(a) shows the powering cycle of the magnet during Phase I of the test. In the same time axis, Fig. 9(b) displays the change in distance, due to a compression, between the endcap nose and the tracker, while in Fig. 9(c) we show the change in the $r\phi$ distance between aligned objects in the first endcap disk. The different distance values measured when the magnet was not powered on are interpreted as a permanent compression/deformation or final closing of the structures.

The quasi-elastic compression is also seen in Figs. 9(b) and (c): changes in distance follow perfectly the current cycle in the solenoid. In Fig. 9(c), the increase in absolute distance represents a deformation of the inner ring in the first endcap disk: the CSC chambers attached to the disk will follow the bending of the iron.

Fig. 10(a) shows the powering cycle of the magnet during Phase II of the test. In the same time axis, Fig. 10(b) shows the measured change of the $r\phi$ distance between alignment objects in the first endcap disk. Note that this measurement corresponds to the one displayed in Fig. 9(c) during Phase I. While the quasi-elastic behaviour following the magnet current is similar as the one observed in Phase I, we do not observe here any permanent effect,

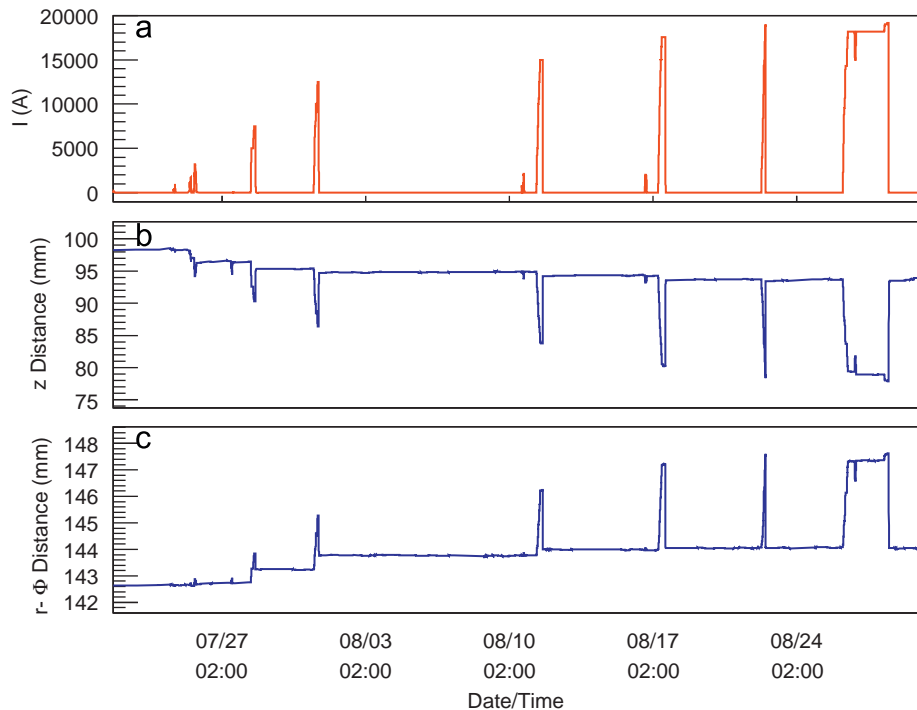


Fig. 9. Illustration of the permanent and quasi-elastic motion cycles during Phase I of the MT (see text).

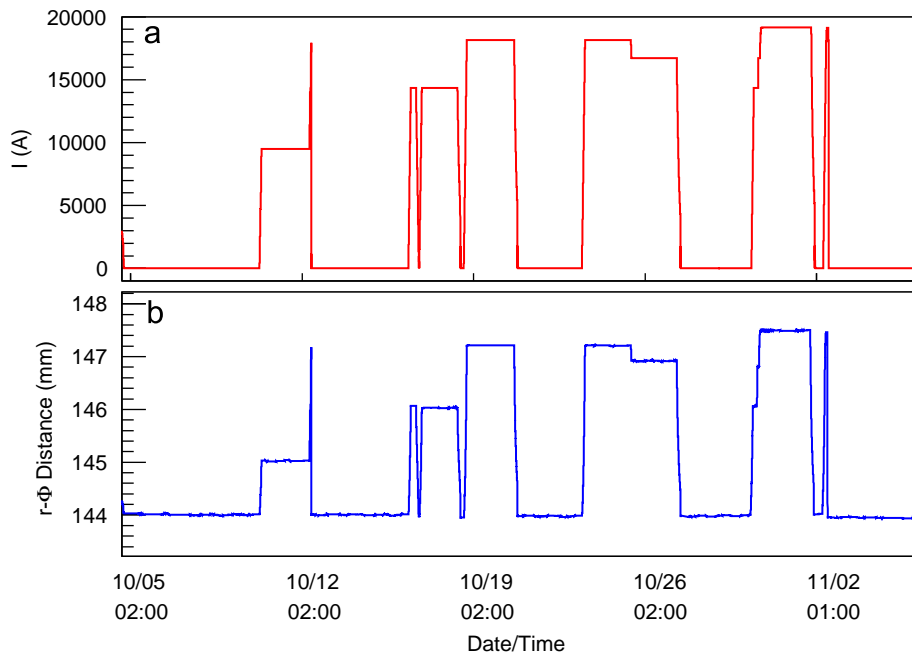


Fig. 10. Illustration of the quasi-elastic motion cycles during Phase II of the MT (see text).

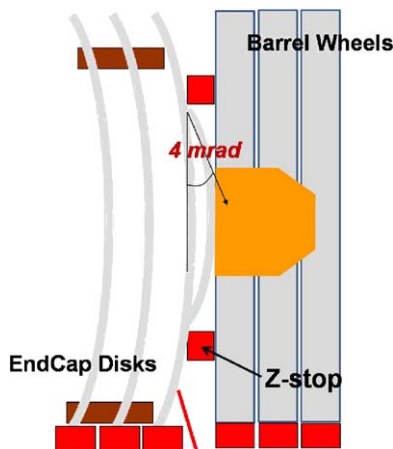


Fig. 11. Sketch of the deformation of the endcap iron disks as a result of the compression due to the magnetic field forces and the resistance of the barrel Z-stops.

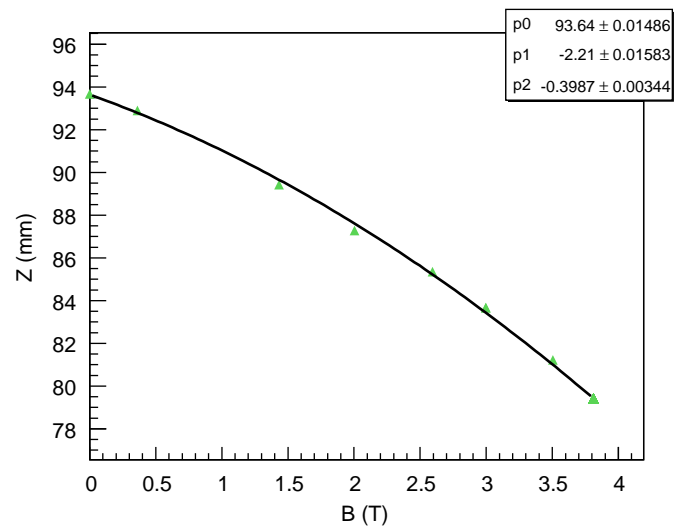


Fig. 12. Results from the relative distance between the first endcap disk and tracker as a function of the magnetic field intensity (see text).

most probably indicating a stable residual deformation of the endcap iron.

We will show later (Section 5.1) that, in fact, there are no purely elastic motions among the CMS elements due to the magnetic field forces, even after the assumed final closing of the detector.

The deformation of the structures due to the magnetic forces is mostly relevant in the endcap disks. The motion of the first endcap disk under the effect of the magnetic forces is, in fact, quite complex. The various Z-stops, which prevent the disks from getting pushed into each other and onto the barrel wheels, cause the endcap disks to bend into a cone shape (see sketch in Fig. 11). The resulting bending angle of the inner ring of the first endcap iron, relative to the vertical, is about 4 mrad.

Figs. 9(a) and 10(a) show the values of the current in the solenoid coils, in A, as a function of the time. For currents in

the range of 4000–19 014 A, the relation between the central magnetic field strength and the current intensity follows a linear expression:

$$B(T) = 0.00020988 \times I(A) + 0.011$$

with an error smaller than 1%.

The observed changes in distance as a function of the magnetic field intensity is dominated by the expected quadratic behaviour. A fraction of the data displayed in Fig. 9(b), corresponding to a run from 0 to 3.8 T, is shown in Fig. 12 as function of the magnetic field.

Using the same set of data we have studied the behaviour with field in separate regions of the detector, with the aim to understand possible asymmetries in $r\phi$. The behaviour is very similar for all the three quadrants.

Apart from effects associated with changes in the magnetic forces, the detector structures are quite stable. Measurements taken during a period of approximately two days at a constant 3.8 T field, with a measured temperature gradient not greater than 2 °C, show stabilities better than 100 μm .

5.1. Discussion on quasi-elastic motions

Given the weights and geometrical dimensions of detector components, the magnitude of the magnetic field forces and the presumably non-negligible friction between touching elements, the property of elasticity is not perfect in the motions of the CMS structures. To illustrate and quantify this effect we have chosen a set of data corresponding to the last part of Phase I of the MT period. For this set of data the detector had already completed its permanent deformations (got mechanically closed) and therefore all observed movements or deformations due to changes in the magnetic forces were considered a priori as quasi-elastic.

The analysed data set corresponds to a run that starts at $B = 0\text{ T}$ and ramps up to 4 T (see Fig. 13(a)), with some intermediate steps where data were recorded at various constant fields, including a long one at 3.8 T.

The top row of Fig. 13 shows the relative distance between the tracker and the first endcap disk for this run as a function of time (Fig. 13(c)), and as a function of the magnetic field (Fig. 13(d)). The middle row shows the $r\phi$ motions of the first inner ring in the YE + 1 disk as a function of time (Fig. 13(b)), and as a function of magnetic field (Fig. 13(e)).

One can easily observe in Fig. 13(c) how the LD stops its approach to the AR and starts to move apart from it when the current intensity decreases, and resumes its displacement towards AR as soon as the current intensity increases again.

Fig. 13(a) shows a change in magnetic field the night from 26/08 to 27/08. The field went from 3.8 T down to 3.2 T and back

up to 3.8 T, after which it remained stable for a long period before the last ramp up to 4 T.

As displayed in Figs. 13(d) and (e) the path 3.8 T–3.2 T–3.8 T, as seen by the sensors monitoring this relative distance, was not elastic. The Δz values at the two 3.8 T positions, in all quadrants, differ by more than 1 mm, while the measured $\Delta r\phi$ values at the two 3.8 T positions differ by more than 0.3 mm.

Moreover, if one restricts the Δz measurements in the region from 0 to 3.8 T and makes a prediction of the expected Δz value extrapolating to 4 T, based on the parameterization shown in Fig. 12, one will make an error greater than half a millimetre.

The non-existence of purely elastic motions shows the difficulty of making any accurate prediction based on previous motion behaviours. Furthermore, the lack of motion reproducibility (equal magnetic forces may result in different motions) will be a constant during CMS operation.

6. Data sets and data quality

Data for the Link alignment system were recorded in continuous mode during the entire MTCC, Phases I and II. In this section we analyse the data quality of the different measurements provided by the system, performing comparisons between the various measurement types and between the two phases of the test. The coherence of the results and reproducibility of the observed measurements are also discussed.

Although each set of data should by itself show the main effects of the magnetic forces acting on detector structures, the exact magnitude of the motions and deformations cannot be directly extracted from the individual sets. A full reconstruction of the detector geometry, as discussed in Section 7, is needed to completely define the system. The reconstruction software, COCOA, uses as input the various raw data we discuss here.

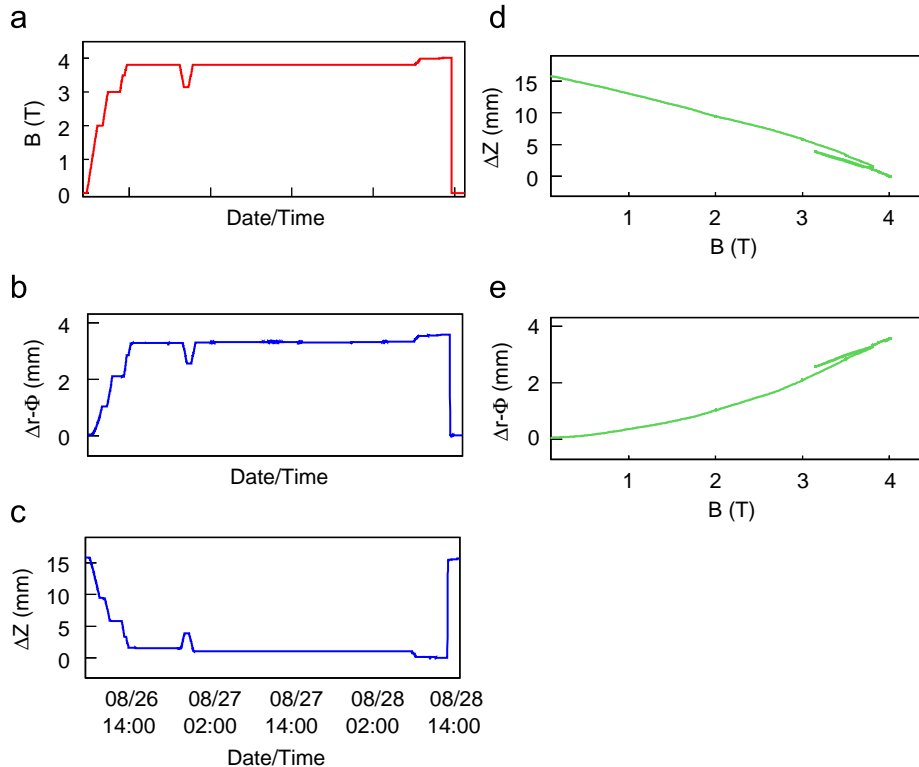


Fig. 13. Illustration of the quasi-elastic motion of the detector at the end of Phase I, in a run to 4 T with a long stability at 3.8 T.

6.1. Laser system and photo-sensors information

The information from the network of lasers is obtained from the analyses of the Amorphous Silicon Position Detector sensors intercepting the light paths. ASPDs are semitransparent 2D position strip sensors constructed on top of a 1 mm thick glass substrate. The active material ($a\text{-Si}_{0.9}\text{C}_{0.1} : \text{H}$, 200 nm thick) is deposited between two layers of perpendicular strip electrodes, 110 nm thick, made of Al-doped ZnO. Each intersection of a top and a bottom ZnO strip defines a Schottky photodiode, formed by the photoconductive material between the ZnO contacts.

There are 64 horizontal and 64 vertical strips. The strip pitch is 430 μm and the strip gap is 22 μm . The strips layout allows having two orthogonal projections of the incoming beam. Vertical strips reproduce the projection of the beam spot along the x-coordinate while horizontal strips reconstruct the y-coordinate. The total active area is $28 \times 28 \text{ mm}^2$.

The centroid corresponding to the laser spot position, at each monitored point in the detector, is reconstructed from Gaussian fits to the two light profile intensities. An example of beam profile

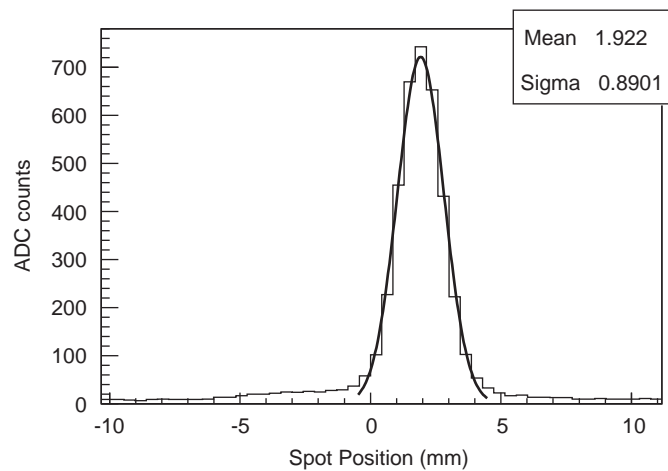


Fig. 14. Gaussian fit of a typical laser spot profile as measured in an ASPD.

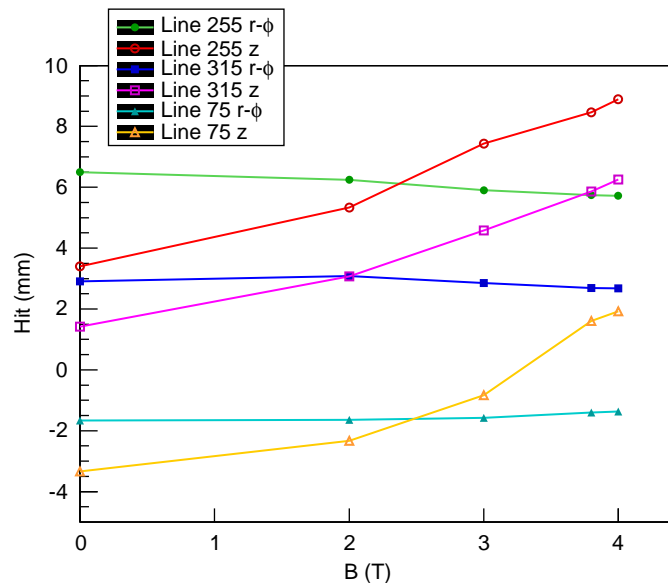


Fig. 15. The z and r laser positions reconstructed by an ASPD for different values of the magnetic field in the three lines.

is shown in Fig. 14. Typical spatial point reconstruction error is of the order of 5 μm in both x and y sensor coordinates.

As an illustration we show, in Fig. 15, the reconstructed laser positions as a function of the magnetic field intensity in a Phase I run where the magnetic field ramped from $B = 0$ to 4 T. The chosen ASPD in the illustration is the one installed at the bottom of the ME1/2 chamber in Fig. 5. The laser beam is the one coming from the LD.

Fig. 15 displays the two reconstructed coordinates, z and $r\phi$, monitored by this sensor in the three equipped quadrants. From these data we can already observe the expected “quasi-quadratic” behaviour with B for the displacements along the CMS z-coordinate, together with a more stable response in the $r\phi$ direction. The behaviour of the reconstructed spot coordinates does not allow by itself a simple interpretation. If the light spot suffers a displacement, the observed motion may be due to a displacement/rotation of the structure to which the sensor is attached, to a motion of the structure holding the laser collimator or, as in most cases, to a combination of both effects.

The reconstructed set of laser light spots on the surfaces of the ASPD sensors are a major input for the reconstruction package. During the test, and for a given magnet condition, not all sensors could be fully reconstructed. This was due to two factors: (a) some of the sensors were damaged during the closing procedure, (b) loss of information due to the limited dynamic range of the system (as defined by the sensor active area), convoluted with the closing tolerance and the significant detector motion with field. This loss of information results in a degradation of the final measurement precision.

6.2. Monitoring of linear displacements

As described in Section 2.4, the measurement of all the degrees of freedom for the different monitored elements in the detector requires a set of extra linear displacement sensors, complementing the laser data. These extra measurements provide information on the coordinates along the light beams, and are input into the global geometry reconstruction fit procedure.

This section presents an independent analysis on the quality of the linear displacement data. We concentrate the study in symmetry, reposition, and reproducibility for different runs.

6.2.1. Axial distance monitoring

Axial (along z) measurements are performed at the inner $\eta = 3$ region and at the outer perimeter of the endcap nose ($r = 2700 \text{ mm}$). Fig. 5 indicates the proximity sensor locations. Table 1 summarizes the results obtained for the inner detector region.

The first row in Table 1 gives the difference between the values of z, at $B = 0 \text{ T}$, before and after a long ramp up to 4 T followed by a fast dump to 0 T. From the inspection of the $\Delta Z(0)$ values, the expected elastic motions are verified, within 3σ in the 75° and 195° regions. At the bottom quadrant the initial LD–AR distance is not retrieved by about half millimetre. This discrepancy will be discussed again in the section devoted to the full geometrical reconstruction of the system. It may be due to the fact that the LD

Table 1
Measured relative displacements along z between the tracker (AR) and ME1 station (LD) during the MT Phase I, for three ϕ positions.

ϕ quarter	75°	195°	315°
$\Delta Z(0 \text{ T}) \text{ (mm)}$	-0.165 ± 0.057	-0.052 ± 0.057	-0.571 ± 0.057
$\Delta Z_{04 \text{ T}} \text{ (mm)}$	-15.741 ± 0.057	-15.540 ± 0.057	-15.599 ± 0.057

is in some sense a floating structure, since it is not physically attached to the YE1 iron disk, but rather hanging from the TPs.

The second row gives the differences between the z measured at $B = 4$ T and the corresponding values at $B = 0$ T, for each of the three ϕ quarters. The three values agree within 3σ .

Axial measurements performed at the outer perimeter of the nose ($r = 2700$ mm) provide information on the behaviour of the ME1/1 disk of chambers with respect to the iron disk supporting the rest of the CSC chambers in the ME1 layer. Table 2 summarizes the results obtained in this region.

In the last three rows of Table 2, we compare the total displacement (ΔZ_{04T}) suffered by the structures, from the beginning of the data taking (at 0 T) to 4 T in both MT Phases. All quantities in Table 2 are given in millimetres. The repositioning and total displacements due to the magnetic forces are compatible, within 3σ , for the three ϕ quarters in both MT Phases.

6.2.2. Radial distance monitoring

Radial ($r\phi$ direction) distance measurements along the radial laser paths combine the information of radial profiles, CSC chamber dimensions, and short range distance measurement sensors. Temperature probes complement long range measurements. Short range radial distance measurements are performed mainly at the inner and outer parts of the ME1/2 ring of chambers. In the inner part of the chambers, measurements are done with respect to the outer perimeter of the nose (TP), while the outer

ME1/2 chamber ring is monitored with respect to the MAB structures. The location of the corresponding proximity sensors is indicated in Fig. 5. Tables 3 and 4 summarize the results.

The comparison between the repositioning $\Delta R(0)$ of the chambers with respect to the nose, before and after the cycle $B = 0, 4$ T and back to $B = 0$ T, measured in Phases I and II, are displayed in the first three rows of Table 3 for the three quadrants in ϕ ($75^\circ, 255^\circ$ and 315°). In the last three rows of Table 3 we compare the total displacement (ΔR_{04T}) suffered by the chambers with respect to the nose during the ramp up from 0 to 4 T in each of the MT Phases. All quantities in Table 3 are given in millimetres. The repositioning and total displacements due to the magnetic forces in the three ϕ lines are compatible between them and with 0 within 1σ in this coordinate.

The results on distance measurements between the ME1/2 ring of chambers and the MAB structures, during the elastic period, are shown in Table 4, for Phases I and II, and for the three ϕ quadrants. For unknown reasons, and during Phase I of the Magnet Test, the sensor located in the MAB at 75° was not working properly.

In the last three rows of Table 4 we compare the total measured displacement (ΔR_{04T}) during the ramp from 0 to 4 T in both MT Phases. As usual, all quantities are given in millimetres. The comparisons between the computed values for repositioning show values compatible with 0 in both MT Phases. The total displacements due to the magnetic forces when reaching $B = 4$ T in the two ϕ regions are compatible within 1σ . The measured radial displacements are compatible with the expected deformations of the ME1/2 chambers due to the Z-stops.

Table 2

Relative displacements (in mm) along z between the YE1(TP) and the ME1/1 ring of chambers measured during both MT Phases (see text).

ϕ quarter	75°	195°	315°
$\Delta Z(0T)$ Phase I	0.091 ± 0.057	0.070 ± 0.057	0.106 ± 0.057
$\Delta Z(0T)$ Phase II	0.029 ± 0.057	0.258 ± 0.057	0.217 ± 0.057
$\Delta Z(0T)$ [Ph. II–Ph. I]	-0.062 ± 0.080	0.188 ± 0.080	0.111 ± 0.080
ΔZ_{04T} Phase I	2.069 ± 0.057	2.789 ± 0.057	2.674 ± 0.057
ΔZ_{04T} Phase II	1.793 ± 0.057	2.734 ± 0.057	2.650 ± 0.057
ΔZ_{04T} [Ph. II–Ph. I]	-0.276 ± 0.080	-0.055 ± 0.080	-0.024 ± 0.080

Table 3

Relative displacements (in mm) along $r\phi$ between the nose (TP) and the inner boundary of ME1/2 chambers measured during both MT phases (see text).

ϕ quarter	75°	255°	315°
$\Delta R(0T)$ Phase I	-0.033 ± 0.057	-0.031 ± 0.057	0.019 ± 0.057
$\Delta R(0T)$ Phase II	-0.040 ± 0.057	0.039 ± 0.057	-0.004 ± 0.057
$\Delta R(0T)$ [Ph. II–Ph. I]	-0.007 ± 0.080	0.070 ± 0.080	-0.023 ± 0.080
ΔR_{04T} Phase I	3.504 ± 0.057	3.839 ± 0.057	3.720 ± 0.057
ΔR_{04T} Phase II	3.502 ± 0.057	3.729 ± 0.057	3.641 ± 0.057
ΔR_{04T} [Ph. II–Ph. I]	-0.002 ± 0.080	-0.110 ± 0.080	-0.079 ± 0.080

Table 4

Relative displacements (in mm) along $r\phi$ between the MAB structures and the ME1/2 ring of chambers measured during both MT phases (see text).

ϕ quarter	75°	255°	315°
$\Delta R(0T)$ Phase I	–	0.0022 ± 0.057	0.000 ± 0.057
$\Delta R(0T)$ Phase II	-0.0073 ± 0.057	-0.057 ± 0.057	-0.198 ± 0.057
$\Delta R(0T)$ [Ph. II–Ph. I]	–	-0.079 ± 0.080	-0.198 ± 0.080
ΔR_{04T} Phase I	–	-2.757 ± 0.057	-2.820 ± 0.057
ΔR_{04T} Phase II	-3.464 ± 0.057	-2.806 ± 0.057	-2.865 ± 0.057
ΔR_{04T} [Ph. II–Ph. I]	–	-0.049 ± 0.080	-0.045 ± 0.080

6.3. Angular monitoring

For the monitoring of the angular motions (small rotations/tilts) of some relevant CMS mechanical structures we use, in the Link alignment system, electrolytic clinometers or tiltmeter sensors (see Section 2.4). Tiltmeters measure the angle, with respect to the gravity vector, of the elements to which they are attached. The precision of these sensors is of the order of $30\text{--}40\ \mu\text{rad}$ [15,16].

Two types of tiltmeters were used during the Magnet Test, 1D and 2D sensors. 1D sensors measure tilts in one direction, while 2D sensors (two 1D on the same mechanical arrangement, and perpendicular to each other) measure tilts in two perpendicular directions.

Dual tiltmeters were installed at the Alignment Ring and Link Disk structures. Monitoring of the ϕ and θ angles in the AR will detect eventual rotations and/or bends of the tracker body or the LD. 1D sensors were installed in the three instrumented MABs. The sensors are placed in a x – y plane in order to register eventual rotations of the structures in that plane. Rotations, if any, will be small variations (μrad) around the nominal ϕ value of the particular MAB structure.

The ϕ monitoring of the AR, with tiltmeters placed at the top and bottom, shows compatibility with no rotation: after the cycle $0T\text{--}4T\text{--}0T$ the ring gets the original orientation within 1σ ($\pm 40\ \mu\text{rad}$). The $\Delta\phi_{04T}$ measured between the orientations at $B = 0$ T and at $B = 4$ T are -0.3 ± 42.4 and $60.0 \pm 56.6\ \mu\text{rad}$ for top and bottom sensors, respectively. Both measurements are compatible with no rotation of the AR.

Concerning the LD, one observes a $\Delta\phi_{04T}$ different from zero in both MT Phases, indicating an apparent anticlockwise rotation around the $+z$ axis of $120.5 \pm 42.4\ \mu\text{rad}$ in Phase I and $108.4 \pm 42.4\ \mu\text{rad}$ in Phase II. This tilt may just reflect the floating character of the LD structure and not a real rotation.

Finally, concerning the MAB structures, we observe no rotations under any magnetic field conditions.

7. Reconstruction results

7.1. Description of the software package

COCOA is an object oriented C++ software to study optical systems through a geometrical approximation based on a non-linear chi squared fit. The software allows the reconstruction of the position and orientation of the optical system objects and the calculation of the propagation of errors. For the CMS Link alignment system, COCOA works with about 30 000 degrees of freedom.

In addition to the measurement files described in Section 4, the system description has to be provided. This includes the interconnection of elements (which laser points to which sensor, for example) and hierarchy (which elements are attached mechanically to which structures), together with an approximation of the geometry obtained from previous measurements (calibrations or photogrammetry). Supplying a good estimate of the geometry is not necessary, but speeds the convergence, ensures the goodness of the result and helps to avoid falling in local minima.

Parameters used by the software are classified as fixed, calibrated and unknown, depending on how the data are used in the fit: as a fixed constant, as coming from calibration (having its corresponding precision) or as unknown and therefore fully free for the minimization. The output from COCOA is the set of parameters which best fit the data.

Let \mathbf{X} be the parameters vector. Elements are X_j , $j = 1, m$. The real measurements associated to vector \mathbf{X} make a system of equations that can be written in a matrix form whose element i is: $M_i = F(x_1, \dots, x_j)$, $i = 1, n$, and $i < j$.

Let \mathbf{P} be the normalized matrix of the errors associated to the real measurements and let \mathbf{D} be the matrix of deviations between real and ideal measurements. What COCOA does is to calculate a new parameters vector \mathbf{X} , correcting its elements in an iterative way, up to convergence to a minimum for the matrix \mathbf{D} .

The corrections to be done on the various parameters are calculated as

$$d\mathbf{X} = (\mathbf{A}^t \times \mathbf{P} \times \mathbf{A})^{-1} (\mathbf{A}^t \times \mathbf{P} \times \mathbf{D}) \quad \text{where } A_{ij} = (\delta M / \delta X_j)_i$$

Once convergence is reached, the vector \mathbf{X} contains the best geometrical description of the system compatible with the measurements and the calibration constants. The propagation errors are contained in the covariance matrix: $C = n^2 (\mathbf{A}^t \times \mathbf{P} \times \mathbf{A})^{-1}$ where n is the matrix \mathbf{P} normalization constant. The correlations between parameters are in the off-diagonal elements.

7.2. Results from COCOA reconstruction

For its use by COCOA, the full system geometry was coded for the MT configuration. It consists of: (a) one Alignment Ring equipped with three lasers pointing to the Link Disk; (b) one Link Disk equipped with three Laser Boxes, each of them (see Fig. 5) containing a splitter which reflects the light coming from the AR and directs it to the MABs, and a laser collimator illuminating the same MAB sensors and, at the same time, providing a parallel light path that impacts on ME1/1 and ME1/2 sensors; (c) three Transfer Plates equipped with three ASPD sensors each; (d) three MABs, each of them containing two ASPD sensors and a laser collimator; (e) three ME1/2 chambers, each of them equipped with two ASPD sensors; (f) three ME1/1 chambers, each of them containing a single ASPD sensor.

Apart from the measurement files corresponding to the 24 ASPD 2D sensors we have included in the reconstruction the data

coming from the proximity sensors (15 in total, see Fig. 5 for their positions and orientations).

An initial geometry was defined based on the calibrated positions and orientations of all the pieces cited above. In order to get the best possible description of the system, an exhaustive use of photogrammetry, laboratory 2D and 3D measurements and calibrations were included in COCOA's description file. The photogrammetry of our system taken at SX5 (see Ref. [17] as reference document) allowed to put in place the main mechanical structures which support the ASPDs and other devices.

Inside these mechanical structures we need to position/orient the actual sensors. This task has been accomplished using 2D high precision (better than 10 μm) measurements of the actual position of the sensor's centre. The 3D precision positioning of a set of predefined pins placed in each mechanics is used to determine more accurately the position of the distancemeters. Finally, the calibrated positions and orientations of all the collimators, together with some optical devices such as rhomboids, were performed at CERN's ISR facilities. Other optical devices present in the system such as pentaprisms were not calibrated before the start of the MT, so an in situ calibration was performed at SX5 once the system was installed and running by direct comparison to photogrammetry data.

7.2.1. Fit at $B = 0\text{ T}$ in Phase I

The reconstruction method chosen was a three-step iteration where in the first step we placed the LD within YE + 1, secondly we attached the MAB structures to the output results of the first step and finally both YE + 1 and YB + 2 are placed in space with respect to the AR.

More precisely, in the first step we assume that all YE + 1 components (ME1/1, ME1/2 and TPs) are placed in their photogrammetric positions and the LD is set as unknown in the reconstruction software. By reconstructing the signals given by the LD lasers over ME1/1, ME1/2 and TP sensors we fit the LD position and orientation. Once the LD is fitted we add to the fit the information from the proximity sensors present in YE + 1 (radial and axial from the TPs and radial from LD to TPs) and let vary, within their calibrated positions, the rest of YE + 1 structures.

Next we proceed to step 2 by fixing all YE + 1 components to their previously fitted values and leaving as unknown the YB + 2 position and orientation, while the MABs are allowed to vary within their calibrated positions inside YB + 2. Performing the reconstruction using the positions of the MAB lasers recorded by the MAB and TP sensors allows the fitting of YB + 2 and the MAB positions and orientations.

Finally in step 3 we fix again the result of the previous fit except for the global positions and orientations of YE + 1 and YB + 2 which are set to calibrated. Furthermore, in this step we allow the collimators from the AR and the splitters placed in the laser boxes of the LD to vary within their calibrated positions. We use now the AR lasers impacting on the TP and MAB sensors.

In order to establish a reference structure in the system description we have chosen the YE + 1 disk placed in x and y and oriented around the z axis as given by survey measurements [18]. Thus we start from a YE + 1 disk placed at $(-1.8, -3.6, 7565)\text{ mm}$ and oriented $(0, 0, 0.43)\text{ mrad}$ around the x , y and z axis, relating the rest of the components to it (the YB + 2 wheel is initially centred at $(0, 0, 5352)\text{ mm}$ and the AR structure at $(0, 0, 2935)\text{ mm}$ both with $(0, 0, 0)$ degrees around x , y and z axis).

One should note that this convention implies that an initial misposition or misorientation of YE + 1 will propagate automatically to the AR and YB + 2 structures not always linearly (for example rotations around the x or y axis of YE + 1 are not equivalent to the same rotations in the AR or YB + 2 disks).

Table 5

Difference in position (in mm) and orientation (in mrad) between the fitted values at $B = 0$ T at the beginning of Phase I using COCOA and the nominal or survey values for YE + 1 and YB + 2.

$B = 0$ T Phase I	Δ_x	Δ_y	Δ_z	Δ_{AngX}	Δ_{AngY}	Δ_{AngZ}
YE + 1	-0.06 ± 0.37	-0.07 ± 0.38	6.50 ± 0.17	0.14 ± 0.07	-0.19 ± 0.07	0.03 ± 0.12
YB + 2	-1.48 ± 0.22	-0.61 ± 0.23	2.99 ± 0.20	0.44 ± 0.07	-0.51 ± 0.07	0.98 ± 0.07

Table 6

Difference in position (in mm) and orientation (in mrad) between the fitted values at $B = 0$ T using COCOA and the survey values from photogrammetry for ME1/1, ME1/2 and MAB structures.

$B = 0$ T Phase I	Δ_x	Δ_y	Δ_z	Δ_{AngX}	Δ_{AngY}	Δ_{AngZ}
ME11-75	-0.09 ± 0.30	-0.05 ± 0.30	-0.49 ± 0.30	–	–	–
ME11-255	0.09 ± 0.30	0.18 ± 0.30	0.59 ± 0.30	–	–	–
ME11-315	-0.01 ± 0.30	0.06 ± 0.30	0.28 ± 0.30	–	–	–
ME12-75	0.26 ± 0.31	0.33 ± 0.41	-0.16 ± 0.30	–	0.00 ± 0.10	0.24 ± 0.10
ME12-255	0.42 ± 0.31	-0.32 ± 0.41	0.05 ± 0.30	–	0.00 ± 0.10	-0.04 ± 0.10
ME12-315	0.13 ± 0.36	-0.60 ± 0.36	0.06 ± 0.30	–	–	–
MAB-75	-0.63 ± 0.40	0.17 ± 0.42	0.84 ± 0.41	–	-0.11 ± 0.11	0.14 ± 0.10
MAB-255	1.46 ± 0.40	0.21 ± 0.41	-0.81 ± 0.42	–	0.73 ± 0.11	-0.51 ± 0.10
MAB-315	-0.83 ± 0.40	-0.37 ± 0.40	-0.00 ± 0.42	–	0.00 ± 0.14	-0.24 ± 0.13

– plain lines indicate degrees of freedom not measured in the fit.

Table 5 shows the difference in position and rotation of the YE + 1 and YB + 2 disks obtained from the fit of the data taken before any magnetic field was applied to the detector (first step). One must take into account that there is no way within the system to distinguish between a real movement of the YB + 2 disk and coordinated movements of the MABs; we have chosen, thus, to assign to the YB + 2 disk the coordinated movements affecting the three MABs and to show separately the individual fitted values for each MAB (thus a comparison with survey data from Ref. [17] may not be direct). One must note that the data used correspond to the first data taken with our system and, as explained in Section 5, the final closure of the detector has not yet happened.

To validate the reconstruction results (output from COCOA), the reconstructed geometry at $B = 0$ T is compared with survey data (when available). The preliminary comparison between fitted and photogrammetry measurements is very good as can be seen in Table 6 for ME1/1 and ME1/2 chamber reference points and for MAB structures. Notice that COCOA uses a convention different from the one used by CMSSW for ME1/1, ME1/2 and MAB reference points, and only relative differences are shown in Table 6. Differences in translation coordinates are in most cases within or close to the $300\mu\text{m}$ accuracy of the photogrammetry measurements for all the structures. These values are also represented in Fig. 16(a).

The goodness of the fit can be obtained by computing the average residual (the difference between the real value measured by a sensor and the fitted value from the intersection of the laser path with this sensor) in each step. In this way an average value of $101.6\mu\text{m}$ is obtained for step 1, of $50.84\mu\text{m}$ for step 2 and $111.9\mu\text{m}$ for step 3. Figs. 16 (b) and (c) show, respectively, the $r\phi$ and z residuals in this last step.

As guidance for the reader we show in Fig. 17 the local coordinates of the endcap chambers and MAB structures with respect to their corresponding wheels.

An important parameter which enters in COCOA's fit is the precision of the measured data. One would tend naively to set this precision as the intrinsic one of the corresponding sensor (either 2D ASPD or 1D distancemeter). However, one should also take into account the quality flag with which the position and orientation of the different mechanical structures are declared in COCOA's description file. More precisely, whenever the positions and

orientations of the structures are declared as unknown within COCOA, the intrinsic precision of the measurements is increased from the nominal values of $10\text{--}300\mu\text{m}$. On the other hand if the position and orientation of the different structures are set to calibrated then the actual error on their calibration (usually $300\mu\text{m}$ for positions and $100\mu\text{rad}$ for orientations) are already taken into account in the error propagation and thus the intrinsic measurement error can be set back to its nominal value.

The data used previously correspond to the first data taken with our system and as explained in Section 5 do not represent the final situation without B field, as a permanent closure of the detector was observed with increased B fields and the initial configuration was not recovered when the field was switched off.

We show in Table 7 the position and orientation of the YE + 1 and YB + 2 structures, endcap chambers and MABs at $B = 0$ T at the end of Phase I after the system has gone through all the variations in magnetic conditions. With these numbers we obtain the final position of the YE + 1 disk (w.r.t. the tracker) with a measured closure along the z axis of 2.58 mm . The changes in the coordinates for the endcap muon chambers can reveal a final adjustment of the mechanical structures or a remaining deformation of the first endcap layer after the magnet cycling.

We compute the plane containing the three ME1/1 chamber reference points (one per chamber) in Table 7 in order to have a quick reference of its change between photogrammetry and our fit. The plane computed directly from photogrammetry values of the reference points in ME1/1 chambers results in a rotation of $360.0\mu\text{rad}$ around the x direction and $-1132.4\mu\text{rad}$ around the y direction w.r.t. its nominal orientation. The same computation with a fit at $B = 0$ T, at the beginning of Phase I, results in a rotation of $543.9\mu\text{rad}$ around the x direction and $-1061.4\mu\text{rad}$ around the y direction (again w.r.t. its nominal orientation).

7.2.2. Fit at $B = 0$ T in Phase II

During the second phase of the MT in October 2006 the AR was extracted from the detector, together with the tracker mock-up. This different configuration of the Link system may induce a different behaviour from that observed in Phase I.

Fits inside YE + 1 and YB + 2 disks can anyhow be performed and compared with those of the previous section. Thus, starting

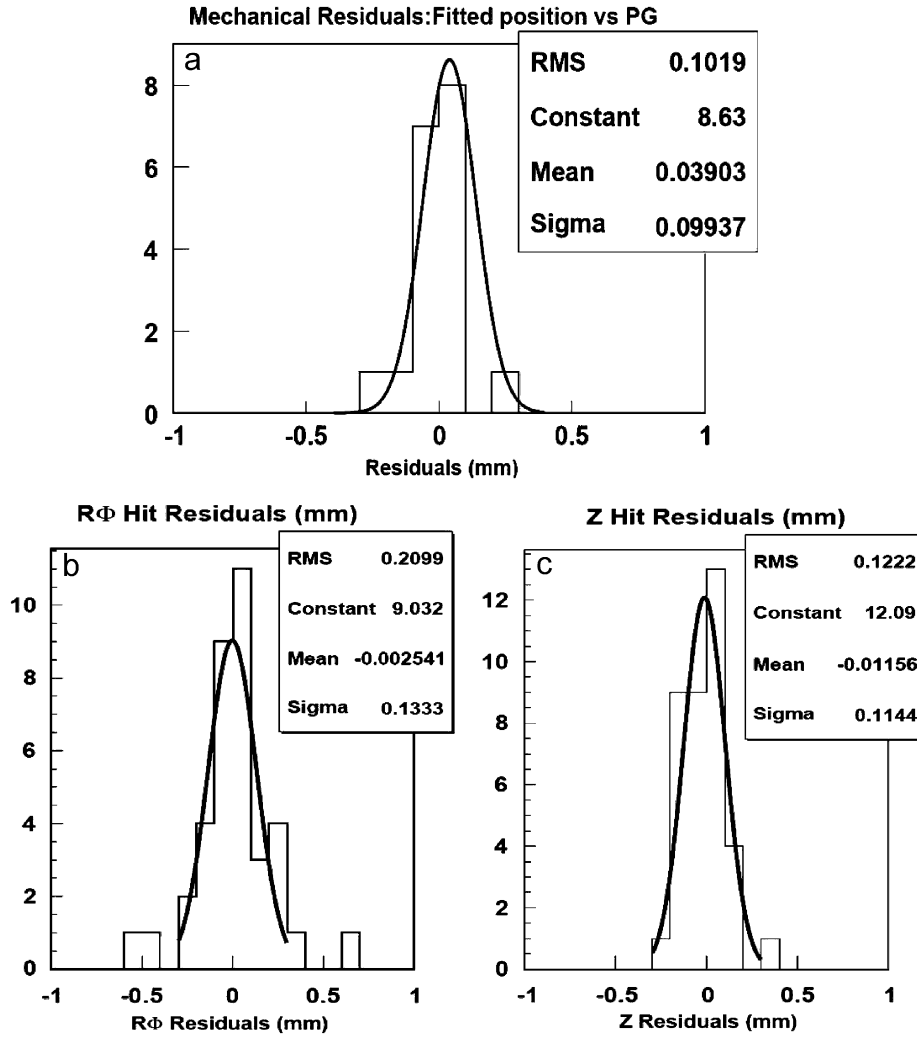


Fig. 16. Mechanical residuals defined as difference in position (in mm) between the fitted values at $B = 0$ T and the survey values from photogrammetry (a) and difference in $r\phi$ and in z between the real value measured by the sensor and the simulated value from the intersection of the laser path with it.

from the situation of the system found at $B = 0$ T at the end of Phase I, a two-step iteration is performed: we place the LD inside YE + 1 in the first step and we attach in a second step the MAB structures to the output of the previous step.

The difference in position and rotation of the YB + 2 disk (also w.r.t. YE + 1) at the beginning of Phase II was calculated, showing a difference in the closing of YE + 1 w.r.t. Phase I of about 1.5 mm in average for all coordinates (note that between phases the endcap was open and closed again).

In a way similar to that of the previous subsection, a cross check of the movements and orientations of the monitored endcap chambers and MAB structures has been performed in this new Phase. The obtained results are compatible with the resolution of 300 μ m quoted above.

7.2.3. Fits with increasing B field in Phase I

Fits to data taken under different magnetic fields were performed in order to compare the variation of positions and orientations monitored by the system. The result of the reconstruction at $B = 0$ T at the end of Phase I was taken as input in the reconstruction program as a better estimation of the geometry.

The comparison of two sets of results monitors the displacements of the different components during the MTCC cycle. At this

point the reference structure chosen as fixed was the AR, which gives a more natural behaviour of the endcap disks approaching the CMS centre when the B field increases. These results show good agreement with the ones discussed in Section 6, and based on the independent analysis of 1D distance sensors. Tables 8 and 9 show, respectively, the difference in position/orientation for the YE + 1 and YB + 2 disks between the data fit at the quoted B field value and the fitted position/orientation at $B = 0$ T in the corresponding magnet run of Phase I.

The average residuals of the fitted values are of 221.4, 229.6, 229.3 and 311.7 μ m for $B = 2, 3, 3.8$ and 4.0 T, respectively, which represent slightly higher values than those obtained with the fits at $B = 0$ T.

As a first preliminary conclusion from these numbers, the compressed distance between YE + 1 and the tracker (or between the Link Disk and the Alignment Ring) can be directly obtained by adding the z shifts towards the CMS centre of the YE + 1 disk and the LD: 13.69 mm (from Table 8) + 1.83 mm (displacement of the LD at 4 T, not shown in the table) = 15.52 mm, which can be compared with the values of the three proximity sensors placed between these two structures at 75°, 195° and 315° giving a compression of 15.6, 15.5, and 15.1 mm, respectively.

As a final summary of the situation of some monitored structures we show in Table 10 the difference in position and orientation for the endcap chambers as well as the MABs between

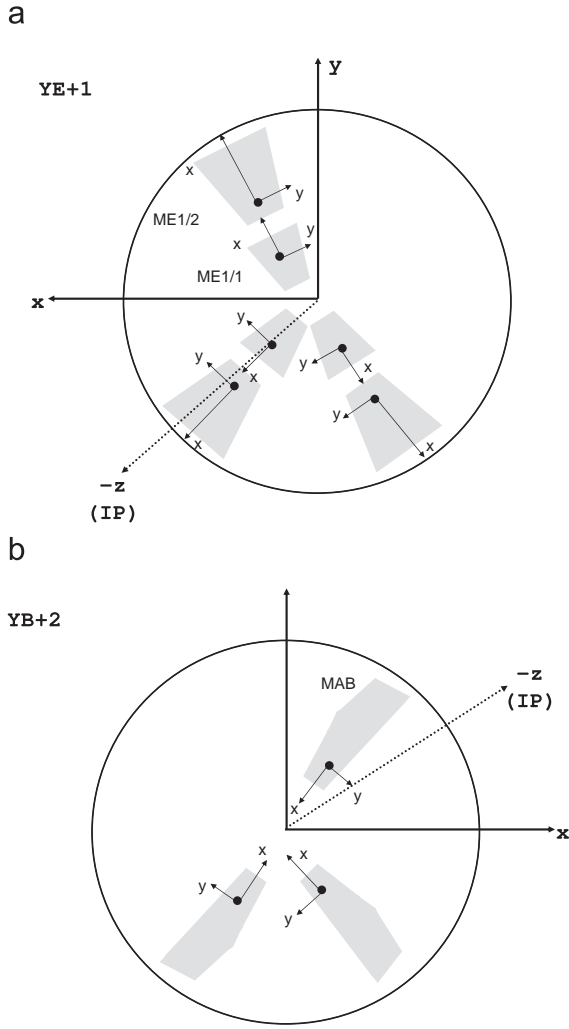


Fig. 17. Local coordinate systems of ME1/1 and ME1/2 chambers in YE + 1 (up) and MAB structures in YB + 2 (down).

Table 7

Difference in position (in mm) and orientation (in mrad) between the fitted values at $B = 0$ T at the end of Phase I using COCOA and those from the beginning for YE + 1, and YB + 2 (w.r.t. the tracker), and for ME1/1, ME1/2 and MAB structures.

$B = 0$ T Phase I	Δx	Δy	Δz	Δ_{AngX}	Δ_{AngY}	Δ_{AngZ}
YE + 1	-0.07 ± 0.21	0.25 ± 0.23	-2.58 ± 0.35	0.24 ± 0.07	0.00 ± 0.07	0.09 ± 0.07
YB + 2	0.18 ± 0.22	-0.42 ± 0.23	0.91 ± 0.37	-0.49 ± 0.07	-0.14 ± 0.07	-0.04 ± 0.07
ME11-75	-0.01 ± 0.41	0.45 ± 0.40	-5.54 ± 0.41	–	–	–
ME11-255	-0.56 ± 0.25	0.60 ± 0.26	1.86 ± 0.27	–	–	–
ME11-315	-0.86 ± 0.23	-0.73 ± 0.25	2.41 ± 0.27	–	–	–
ME12-75	0.88 ± 0.32	1.78 ± 0.62	-2.97 ± 0.29	–	0.31 ± 0.06	-0.11 ± 0.05
ME12-255	-1.48 ± 0.31	-0.64 ± 0.54	1.59 ± 0.41	–	-1.29 ± 0.06	-0.24 ± 0.05
ME12-315	1.13 ± 0.42	-0.65 ± 0.42	2.82 ± 0.27	–	–	–
MAB-75	0.66 ± 0.50	-0.17 ± 0.74	-3.51 ± 0.62	–	0.40 ± 0.08	0.00 ± 0.07
MAB-255	-0.94 ± 0.43	-0.18 ± 0.53	0.76 ± 0.59	–	0.61 ± 0.07	-0.05 ± 0.07
MAB-315	0.98 ± 0.53	-0.62 ± 0.53	2.75 ± 0.65	–	0.30 ± 0.17	0.05 ± 0.16

– plain lines indicate degrees of freedom not measured in the fit.

Table 8

Difference in position (in mm) and orientation (in mrad) between the fitted values at the quoted B field and $B = 0$ T at the end of Phase I using COCOA for the YE + 1 Disk (w.r.t. tracker).

YE + 1 Phase I	Δx	Δy	Δz	Δ_{AngX}	Δ_{AngY}	Δ_{AngZ}
$B = 2$ T	1.54 ± 0.26	-0.71 ± 0.26	-5.18 ± 0.32	0.04 ± 0.07	0.05 ± 0.09	0.22 ± 0.07
$B = 3$ T	1.44 ± 0.26	-0.61 ± 0.26	-8.98 ± 0.32	-0.05 ± 0.07	0.00 ± 0.09	0.23 ± 0.07
$B = 3.8$ T	1.07 ± 0.26	-0.42 ± 0.26	-13.03 ± 0.32	0.04 ± 0.07	0.00 ± 0.09	-0.04 ± 0.07
$B = 4.0$ T	1.22 ± 0.26	-0.39 ± 0.26	-13.69 ± 0.32	0.04 ± 0.07	0.44 ± 0.09	0.07 ± 0.07

the fitted values at $B = 3.8$ T using COCOA and the corresponding values at $B = 0$ T. One should note that a distancemeter in the MAB structure placed at 75° did not work properly during part of Phase I, so no sensible values for the x and y coordinates can be obtained.

As an example, we show in Table 11 the follow up of the motion with field for one of the endcap muon chambers. A similar behaviour is observed for the rest of the monitored units.

7.2.4. Fits with increasing B field in Phase II

Similarly to the $B = 0$ T case, we have fitted the system with the different magnetic conditions of Phase II. Not having the AR as a reference structure implies that the relative movements obtained will be between the YE + 1 and YB + 2 disks. We have chosen in these fits to set YE + 1 as fixed. Table 12 shows the difference in position/orientation for the YB + 2 disk (w.r.t. YE + 1) for increasing B field values with respect to the $B = 0$ T situation after the permanent closure of the detector.

The main displacements (affecting the z coordinates) result in a good agreement with what has been obtained in Phase I taking into account that in this case we are showing relative movements of YB + 2 with respect to YE + 1 (which has been fixed at $z = 7565$ mm). As an example, the z relative distance in Phase II at $B = 3.8$ T between YB + 2 and YE + 1 is of 862.86 mm and should be compared with a distance in Phase I of 862.89 mm. The average residuals of the fitted values in this case are of 121.13, 106.01, 108.7 and 121.2 μ m for $B = 2, 3, 3.8$, and 4 T, respectively.

As a further study of the reproducibility of motion with field, we show in Table 13 the same study as presented in Table 11, for one of the endcap chambers. The behaviour observed in Phase I is very well reproduced with Phase II data.

8. Summary and conclusions

A test of part of the CMS muon alignment system was performed in summer and autumn 2006 as part of the first

Table 9
Difference in position (in mm) and orientation (in mrad) between the fitted values at the quoted B field and $B = 0$ T at the end of Phase I using COCOA for the YB + 2 Disk (w.r.t. the tracker).

YB + 2 Phase I	Δ_x	Δ_y	Δ_z	Δ_{AngX}	Δ_{AngY}	Δ_{AngZ}
$B = 2$ T	0.81 ± 0.35	-0.24 ± 0.38	-0.58 ± 0.63	-0.51 ± 0.09	0.23 ± 0.12	0.35 ± 0.08
$B = 3$ T	1.28 ± 0.35	1.26 ± 0.38	-0.14 ± 0.63	-0.30 ± 0.09	0.91 ± 0.12	-0.07 ± 0.08
$B = 3.8$ T	1.00 ± 0.35	1.37 ± 0.38	-0.37 ± 0.63	-0.51 ± 0.09	1.27 ± 0.12	-0.37 ± 0.08
$B = 4.0$ T	1.21 ± 0.35	2.28 ± 0.38	-0.03 ± 0.63	-0.63 ± 0.09	1.71 ± 0.12	-0.33 ± 0.08

Table 10
Difference in position (in mm) and orientation (in mrad) between the fitted values at $B = 3.8$ T in Phase I using COCOA and $B = 0$ T for ME1/1, ME1/2 and MAB structures.

$B = 3.8$ T Phase I	Δ_x	Δ_y	Δ_z	Δ_{AngX}	Δ_{AngY}	Δ_{AngZ}
ME11-75	1.60 ± 0.34	-0.09 ± 0.27	-2.36 ± 0.39	–	–	–
ME11-255	0.08 ± 0.31	0.97 ± 0.28	-2.67 ± 0.36	–	–	–
ME11-315	-0.36 ± 0.28	-0.51 ± 0.29	-1.22 ± 0.35	–	–	–
ME12-75	2.02 ± 0.38	-1.82 ± 0.78	1.97 ± 0.39	–	-3.87 ± 0.72	-0.38 ± 0.69
ME12-255	-0.84 ± 0.34	-2.00 ± 0.64	1.45 ± 0.36	–	-3.91 ± 0.72	-0.35 ± 0.69
ME12-315	0.21 ± 0.50	-0.80 ± 0.50	3.10 ± 0.35	–	–	–
MAB-75	–	–	1.49 ± 0.76	–	-0.44 ± 0.08	-0.32 ± 0.08
MAB-255	1.25 ± 0.50	-1.18 ± 0.66	-4.16 ± 0.70	–	0.28 ± 0.16	-0.10 ± 0.16
MAB-315	-0.13 ± 0.67	-0.27 ± 0.64	2.67 ± 0.73	–	0.32 ± 0.19	-0.12 ± 0.19

– plain lines indicate degrees of freedom not measured in the fit.

Table 11
Difference in position (in mm) and orientation (in mrad) between the fitted values at the quoted B field in Phase I and $B = 0$ T using COCOA for the ME1/2 chamber placed at 255° (w.r.t. YE + 1).

ME12-255 Phase I	Δ_x	Δ_y	Δ_z	Δ_{AngX}	Δ_{AngY}	Δ_{AngZ}
$B = 2$ T	1.10 ± 0.34	-2.15 ± 0.64	-0.31 ± 0.36	–	-1.68 ± 0.07	0.23 ± 0.07
$B = 3$ T	0.10 ± 0.34	-1.68 ± 0.64	0.21 ± 0.36	–	-2.71 ± 0.07	-0.14 ± 0.07
$B = 3.8$ T	-0.84 ± 0.34	-2.00 ± 0.64	1.45 ± 0.36	–	-3.91 ± 0.07	-0.35 ± 0.07
$B = 4.0$ T	-0.75 ± 0.34	-1.73 ± 0.64	1.06 ± 0.36	–	-4.01 ± 0.07	-0.35 ± 0.07

Table 12
The difference in position (in mm) and orientation (in mrad) between the fitted values at the quoted B field values in Phase II and $B = 0$ T using COCOA for the YB + 2 Disk (w.r.t. YE + 1).

YB + 2 Phase II	Δ_x	Δ_y	Δ_z	Δ_{AngX}	Δ_{AngY}	Δ_{AngZ}
$B = 2$ T	0.05 ± 0.36	-0.34 ± 0.38	5.12 ± 0.67	-0.42 ± 0.10	-0.23 ± 0.12	-0.22 ± 0.10
$B = 3$ T	0.06 ± 0.36	-0.26 ± 0.38	8.70 ± 0.67	-0.63 ± 0.10	-0.37 ± 0.12	-0.02 ± 0.10
$B = 3.8$ T	-0.02 ± 0.36	-0.17 ± 0.38	13.30 ± 0.67	-0.72 ± 0.10	-0.31 ± 0.12	0.07 ± 0.10
$B = 4$ T	-0.09 ± 0.36	-0.17 ± 0.38	14.34 ± 0.67	-0.70 ± 0.10	-0.09 ± 0.12	-0.19 ± 0.10

Table 13
Difference in position (in mm) and orientation (in mrad) between the fitted values at the quoted B field in Phase II and $B = 0$ T using COCOA for the ME12 chamber placed at 255° (w.r.t. YE + 1).

ME12-255 Phase II	Δ_x	Δ_y	Δ_z	Δ_{AngX}	Δ_{AngY}	Δ_{AngZ}
$B = 2$ T	-0.96 ± 0.38	-0.71 ± 0.63	0.27 ± 0.38	–	-1.89 ± 0.08	-0.28 ± 0.07
$B = 3$ T	-0.18 ± 0.38	-1.48 ± 0.63	0.87 ± 0.38	–	-3.12 ± 0.08	0.11 ± 0.07
$B = 3.8$ T	-0.37 ± 0.38	-1.94 ± 0.63	1.74 ± 0.38	–	-4.23 ± 0.08	0.09 ± 0.07
$B = 4.0$ T	-0.71 ± 0.38	-2.01 ± 0.63	1.18 ± 0.38	–	-4.57 ± 0.08	-0.09 ± 0.07

commissioning of the four-Tesla Magnet. The test (Magnet Test and Cosmic Challenge) took place in the SX5 CMS assembly Hall at CERN. About 5% of the muon detector was also commissioned with cosmic rays.

A quarter of the Link alignment system was installed and operated during the test. The readout electronics, DAQ and detector

control systems, integrated into the DCS (Detector Control System) environment, were also successfully tested. The reconstruction procedure was established and for the first time applied to a sizable set of data recorded by the system. Calibrations of individual sensors and laser holder structures, 3D measurements of sensor mounts and associated mechanics, and survey and photogrammetry

measurements of the installed components were analysed and input into the geometry reconstruction software.

The reconstruction of the 3D geometry of this system has been validated by means of a cross-check of data reconstruction at $B = 0\text{ T}$ against photogrammetry and survey data of some reference points, resulting in a good understanding of the system. Furthermore, data taken by the system were analysed at different field conditions and in the two Phases of the MT to get an estimate of the global movements of different detector structures like endcap or barrel disks, allowing as well a crosscheck of the soundness of the results between the different conditions.

We have shown in this note a global fit of the Link alignment system in Phases I and II of the MT. Both phases differ basically in the absence of the AR in the second phase of the MT. Due to the fact that the AR is used as our reference frame, its absence heavily influences the final position of the $\text{YE} + 1$ and $\text{YB} + 2$ disks. The AR suffered two unforeseen displacements (due to technical interventions) during Phase I of the MT. Even though we have tried to fix each time the new position and orientation of the AR structure, residual effects may still appear in the final fitted position or orientation of big structures.

With increasing B field, the behaviour of $\text{YE} + 1$ follows the expected movement towards the CMS centre with a maximum displacement of 13.69 mm. ME1/2 chambers placed inside this disk suffer from a global displacement and a rotation around their local y axis. According to these values, the chambers do not follow completely the $\text{YE} + 1$ displacement (its local z would be zero) but are left behind by 1–4 mm depending on the chamber and the considered Phase of the MT. In addition, the chambers experience a tilt of up to 4.3 mrad (the external region of the chambers are displaced towards positive z). The picture resulting from these ME1/2 chamber motions is in agreement with that found by the endcap optical system as presented in Refs. [8,9]. This first comparison between two different approaches can be considered as an important milestone of the MT alignment exercise.

In agreement with the design requirements, the Link system obtains geometrical reconstructions of relative spatial locations and angular orientations between the muon chambers and the tracker body with a resolution better than $150\text{ }\mu\text{m}$ for distances and $\sim 40\text{ }\mu\text{rad}$ for angles.

Acknowledgements

The authors gratefully acknowledge all the people who worked during the Magnet Test and Cosmic Challenge of the CMS detector. The support and collaboration of the CERN Survey Group are greatly appreciated.

References

- [1] The CMS Collaboration, The CMS experiment at the CERN LHC, J. Instr. 3 (2008) S08004.
- [2] The CMS Collaboration, The Magnet Project Technical Design Report, CERN/LHCC 97-10, 1997.
- [3] The CMS Collaboration, The Muon Project Technical Design Report, CERN/LHCC 97-32, 1997.
- [4] V. Karimaki, G. Wrochna, CMS TN/94-199, 1994; F. Matorras, A. Meneguzzo, CMS TN/95-069, 1995; I. Belotelov, et al., CMS Note 2006/017, 2006.
- [5] The CMS Magnet Test and Cosmic Challenge (MTCC Phase I and II), Operational Experience and Lessons Learnt, CERN/LHCC 2007-011, LHCC-G-129, CMS Note 2007/005, March 7, 2007.
- [6] P. Arce, A.L. Virto, CMS Object Oriented Code for Optical Alignment (COCOA), CMS Note 2002/060, 2002.
- [7] The CMS Collaboration, The Tracker Project Technical Design Report, CERN/LHCC 98-06, 1998.
- [8] M. Hohlmann, et al., Design and performance of the alignment system for the CMS muon endcaps, in: Proceedings of the IEEE Nuclear Science Symposium, San Diego, V.1, 2006, pp. 489–495; CMS CR 2008/016, 16 May 2008.
- [9] M. Hohlmann et al., Aligning the CMS muon endcap detector with a system of optical sensors, in: Proceedings of the IEEE Nuclear Science Symposium, Honolulu, V.1, 2007, pp. 657–662 and CMS CR 2008/015, 16 May 2008.
- [10] A. Calderón, et al., Nucl. Instr. and Meth. A 565 (2006) 603.
- [11] A. Calderón, et al., Amorphous Silicon Position Detectors for the Link Alignment System of the CMS Detector: Users Handbook, CIEMAT 1126, December 2007.
- [12] Sakae Tsushin Kogyo Co., Ltd., Trade Department, 322 Ichinotsubo, Nakahara-ku, Kawasaki, Kanagawa, Japan (<http://www.sakae-tsushin.co.jp>).
- [13] Omron Corporation, Tokyo Head Office, 3-4-10 Toranomon Minato-ku, Tokyo 105, Japan (<http://www.omron.com>).
- [14] J. Alberdi, et al., Proximity sensors Link Alignment System of the CMS Experiment: Users Handbook, CIEMAT, to be published.
- [15] Applied Geomechanics Incorporated, 1336 Brommer Street, Sanya Cruz, CA, USA (<http://www.geomechanics.com/>).
- [16] J. Alberdi, et al., Tiltmeters for the Alignment System of the CMS Experiment: Users Handbook, CIEMAT 1107, May 2007.
- [17] J.F. Fuchs, R. Goudard, J.D. Maillefaud, CMS-YE + 1 Photogrammetry of the $\text{YE} + 1$, CMS-SG-UR-0058.
- [18] J.F. Fuchs, R. Goudard, J.D. Maillefaud, CMS-SUMMARY. YBs and YEs Position w.r.t. YB0 in SX5, CMS-SG-UR-0490.